High-resolution X-ray Luminescence Extension Imaging

Xiangyu Ou[1,†], Xian Qin[2,†], Bolong Huang[3,†], Jie Zan[1], Qinxia Wu[1], Zhongzhu Hong[1], Lili Xie[1], Hongyu Bian[2], Zhigao Yi[2], Xiaofeng Chen[1], Yiming Wu[2], Xiaorong Song[1], Juan Li[1], Qiushui Chen[1,5*], Huanghao Yang[1,5*] & Xiaogang Liu[2,4,6*]

[1]*MOE Key Laboratory for Analytical Science of Food Safety and Biology & State Key Laboratory of Photocatalysis on Energy and Environment, College of Chemistry, Fuzhou University, Fuzhou 350108, China.* [2]*Department of Chemistry, National University of Singapore, Singapore 117543, Singapore.* [3]*Department of Applied Biology and Chemical Technology, The Hong Kong Polytechnic University, Hong Kong SAR, China.* [4]*Joint School of National University of Singapore and Tianjin University, International Campus of Tianjin University, Binhai New City, Fuzhou 350207, China.* [5]*Fujian Science & Technology Innovation Laboratory for Optoelectronic Information of China, Fuzhou 350108, P. R. China.* [6]*Center for Functional Materials, National University of Singapore Suzhou Research Institute, Suzhou 215123, China.*

*Corresponding author. E-mail: qchen@fzu.edu.cn (Q.C.); hhyang@fzu.edu.cn (H.Y.); chmlx@nus.edu.sg (X.L.)

[†]These authors contributed equally to this work.

Current X-ray imaging technologies involving flat-panel detectors have difficulty in imaging three-dimensional (3D) objects because fabrication of large-area, flexible silicon-based photodetectors on highly curved surfaces remains a challenge[1-3]. Here we demonstrate ultralong-lived X-ray trapping for flat-panel-free, high-resolution 3D imaging using a series of solution-processable, lanthanide-doped nanoscintillators. Corroborated with quantum mechanical simulation, our experimental characterizations show that a thermally activated slow-hopping of trapped electrons, due to radiation-induced anionic migration in host lattices, induces more than 30 days of persistent radioluminescence. We further demonstrate X-ray luminescence extension imaging (Xr-LEI) with >20-lp/mm resolution and >15-day optical memory. These findings provide insight into mechanisms underlying X-ray energy conversion through enduring electron trapping and also offer a new paradigm to motivate future research in wearable X-ray detectors for patient-centered radiography and mammogram, imaging-guided therapeutics, high-energy physics, and deep learning in radiology.

Flat-panel X-ray detectors with active readout mechanisms have found critical applications in medical diagnostics, security screening, and industrial inspection[4]. Over recent decades, several types of X-ray detectors, mainly based on direct conversion of X-ray energy into electrical charges or indirect conversion using a scintillating material, have been implemented[5-8]. Many X-ray detection technologies require integration of flat-panel detectors with thin-film transistors (TFT) consisting of pixelated photodiode arrays deposited on glass substrates. Although TFT-integrated flat-panel detectors offer high sensitivity for X-ray detection and radiographic reconstruction, they present substantial challenges for high-resolution X-ray imaging. Apart from high device costs, flat-panel detectors are not applicable to 3D X-ray imaging of curved or irregularly-shaped objects. Despite enormous efforts, flexible X-ray detectors have not been developed due to stringent dual requirements of a flexible TFT substrate and a thin layer of scintillators conformably attached to the flexible substrate.

Persistent luminescent phosphors can store excitation energy and slowly release the captured energy as light emissions[9-12], making it possible to develop flat-panel-free, X-ray detectors. Although inorganic oxide phosphors, such as $SrAl_2O_4:Eu^{2+}/Dy^{3+}$ and $ZnGa_2O_4:Cr^{3+}$ (ZGO:Cr) have been used for *in vivo* optical imaging under X-ray irradiation[13], these materials suffer from low X-ray sensitivity[14]. Moreover, their fabrication also requires complex crystal growth processes under harsh conditions (> 600 °C) to generate efficient electron-trapping states in host lattices[15]. Persistent luminescent microparticles can be prepared by mechanical grinding[12]. However, microparticles are difficult to disperse in solution for thin-film processing, a prerequisite for fabrication of flexible devices.

Lanthanide-doped materials that exhibit unique luminescence properties[16, 17] have been widely used in X-ray scintillation[3, 18-20], optical imaging[21, 22], biosensing[23], and optoelectronics[24]. Notably, high-energy irradiation can displace small anions from their lattices to interstitial sites, creating vacancies and interstitial pairs[25]. We reasoned that generation of persistent luminescence is possible using X-ray-excited lanthanide-doped fluoride nanocrystals, as a result of high-efficiency trapping of electrons and holes due to facile fluoride ion migration. Here, we report a general approach for flat-panel-free X-ray imaging of 3D electronic objects using lanthanide-doped nanoscintillators that feature high-efficiency X-ray absorption and long-lived energy trapping. We name this imaging

technology as X-ray luminescence extension imaging (Xr-LEI) for its ability to attach nanocrystal-based X-ray detectors conformally to highly curved 3D objects for high-resolution, large-area 3D radiography, which is inaccessible by conventional flat-panel X-ray detectors or synchrotron-based X-ray microscopy.

We synthesized a series of terbium (Tb^{3+})-doped $NaLuF_4$ nanoscintillators by a co-precipitation method[22] (Extended Data Figs. 1 & 2). A representative transmission electron micrograph (TEM) of oleic acid-capped $NaLuF_4$:Tb (15 mol%)@$NaYF_4$ core-shell nanoscintillators reveals a hexagonal shape with an average size of 27 nm (Fig. 1a). The radioluminescence of $NaLuF_4$:Tb@$NaYF_4$ nanoscintillators was measured under excitation with a 50-kV X-ray source (Fig. 1b). We observed a set of intense emission bands, corresponding to $^5D_4{\rightarrow}^7F_4$ (584 nm), $^5D_4{\rightarrow}^7F_5$ (546 nm), and $^5D_4{\rightarrow}^7F_6$ (489 nm) optical transitions of Tb^{3+}. On switching off the X-ray source, we recorded prolonged radioluminescence decay of these nanoscintillators with gradually decreasing intensity (Figs. 1b & 1c; Extended Data Fig. 3; Supplementary Movie 1), suggesting effective trapping of ionizing radiation. Intriguingly, the afterglow emission of $NaLuF_4$:Tb@$NaYF_4$ nanoscintillators lasted more than 30 days after switching off the X-ray source (Fig. 1b, bottom). By comparison, the afterglow lifetime of previously reported $ZnGa_2O_4$:Cr^{3+} phosphors is approximately 15 days[12]. We also observed a gradual increase in the emission intensity of $NaLuF_4$:Tb@$NaYF_4$ nanoscintillators on continuous X-ray irradiation, indicating a dynamic energy-charging process (Extended Data Fig. 3). Importantly, our nanomaterials cannot be activated by daylight, making them ideal for fabrication of X-ray memory devices. Notably, coating of a $NaYF_4$ shell onto $NaLuF_4$:Tb nanoparticles enhanced the radioluminescence intensity by 1.5-fold, while the afterglow luminescence intensity was increased by 6.5-fold (Fig. 1c). These results suggest that $NaYF_4$-shell passivation can effectively mitigate quenching of trapped X-ray energies on nanocrystal surfaces. (Extended Data Fig. 3).

We next benchmarked the radioluminescence performance of $NaLuF_4$:Tb (15 mol%)@$NaYF_4$ nanoscintillators with commerical plastic scintillators and several conventional persistent phosphors, including $SrAl_2O_4$:Eu^{2+}/Dy^{3+} powder, ZnS:Cu^{2+}/Co^{2+} powder, $SrAl_2O_4$:Eu^{2+}/Dy^{3+} nanoparticles, and $ZnGa_2O_4$:Cr^{3+} nanoparticles. Under X-ray irradiation at 50 kV, our core-shell nanoscintillators exhibited much stronger X-ray-induced emission and afterglow luminescence than commercial counterparts (Fig. 1d; Extended Data Figs. 4 & 5; Extended Data Table 1). Improvements in

performance were attributed to the large X-ray stopping power and high X-ray trapping efficiency of NaLuF$_4$:Tb@NaYF$_4$ nanoscintillators. These oleic acid-capped nanoscintillators emit radioluminescence visible to the unaided eye upon switching off the X-ray source (70 kV, 1 mA) (Fig. 1e). Moreover, multicolor radioluminescence modulation from the ultraviolet/visible to the near-infrared (NIR) can be achieved using hexagonal-phase NaLuF$_4$ nanocrystals as a host material for activator doping (e.g., Nd^{3+}, Tm^{3+}, Dy^{3+}, Tb^{3+}, Er^{3+}, Ho^{3+}, Sm^{3+} and Pr^{3+}) (Fig. 1f; Extended Data Fig. 6). Notably, there is no detectable afterglow luminescence from Eu^{3+}-doped nanoparticles after X-ray charging (Extended Data Fig. 7).

To understand how large-momentum X-ray photons interact with lanthanide-doped nanoscintillators to produce lasting radioluminescence, we examined the X-ray photon-absorbing ability of the NaLuF$_4$ host. The absorption coefficient of NaLuF$_4$ (the highest atomic number Z_{max} = 71, K_α = 63.31 keV) is much larger than that of NaYF$_4$ (Z_{max} = 39, K_α = 17.05 keV) or NaGdF$_4$ (Z_{max} = 64, K_α = 50.24 keV) (Fig. 2a)[26]. Indeed, the afterglow intensity of NaLuF$_4$:Tb (15 mol%) nanocrystals is 3-fold stronger than that of NaYF$_4$:Tb (15 mol%) nanocrystals, suggesting the effect of heavy atoms (e.g., Lu^{3+}) on X-ray absorption (Fig. 2b). We argue that the high-efficiency radioluminescence should be attributed to not only strong X-ray absorption as a result of heavy atom effect (Extended Data Fig. 7), but also the low-phonon energy of the hexagonal-phase NaLuF$_4$ crystal lattice (< 350 cm^{-1}) as well as reduced surface quenching due to shell passivation. Moreover, at a low Gd^{3+} concentration (< 30 mol%), the excitation energy can be efficiently transferred from Gd^{3+} to Tb^{3+} or Er^{3+} activators. By comparison, at a high Gd^{3+} concentration (> 30 mol%), the excitation energy dissipates nonradiatively to quenching sites through energy migration, resulting in low afterglow intensity of Tb^{3+} or Er^{3+} with fast spontaneous emission (Extended Data Fig. 7).

We further investigated long-lived, X-ray energy trapping by modeling the formation of Frenkel defects in a NaLuF$_4$ lattice. We speculated that a sufficient intensity may dislocate fluoride lattice ions (F$^-$) to interstitial sites through elastic collisions with large-momentum X-ray photons[25, 28] (Extended Data Fig. 8). This leads to formation of fluoride vacancies (V$_F$) and interstitials (I$_F$), accompanied by production and trapping of many energetic electrons (e$^-$) in Frenkel defect-associated trap states. Using first-principles calculations based on density functional theory (DFT), we monitored the structural relaxation of anion Frenkel pairs at various distances. We found

that interstitial defects gradually diffuse to original fluoride vacancies if the proximity of these two sub-defects is less than 3 Å. For defect pairs with a larger separation (> 3 Å), interstitial fluoride ions can be stabilized due to increased energy barriers, except under stimulation with heating or light exposure. Creation of such defect pairs requires formation energies from 2.78 to 12 eV, suggesting a high probability of displacing fluoride ions upon X-ray irradiation (Fig. 2c). Moreover, DFT calculations reveal that for defect pairs with small separation distances, electron relaxation and atom diffusion have similar rates (Extended Data Fig. 8). With an increase in separation distance, the rate of electron relaxation decreases, due to substitution-based anion diffusion, rather than direct relaxation.

We next examined the transient dynamics of X-ray energy trapping at Frenkel defects by varying the X-ray dosage. Our experiments indicated that afterglow intensity can be enhanced with higher doses, which increase electron traps for X-ray energies (Fig. 2d). We further measured captured electrons at trap states by electronic paramagnetic resonance (EPR) spectroscopy. After stoppage of X-ray excitation, we observed a gradual decrease in EPR signal intensity ($g = 1.8743$ and $g = 2.1163$), and the EPR signal completely disappeared upon heating at 200 ºC for 20 min (Fig. 2e). These results confirm that it is possible to generate high-density Frenkel traps in lanthanide-doped nanoscintillators using high-momentum X-ray photons and subsequently to achieve long-lived photon trapping.

In light of experimental and computational results, we proposed the following mechanism underlying long-lived photon trapping in lanthanide-doped nanoscintillators (Fig. 3a). In a $NaLuF_4$:Tb (15 mol%) nanoscintillator, X-ray energies are absorbed by lattice atoms to create many energetic electrons, largely due to photoelectric effects. Through elastic collisions of large-momentum X-ray photons with small fluoride ions, anion Frenkel defects are formed simultaneously in the nanocrystal to trap thermalized low-energy electrons, enabling long-lived photon trapping. Specifically, fluoride vacancies and interstitials are created as electron traps (E-trap) and hole traps (H-trap) (Extended Data Fig. 8), and displacements of fluoride ions at short and long distances form transient shallow and long-lived deep trap states, respectively. Electrons in shallow traps can spontaneously escape over time to the conduction band with a concurrent defect self-healing process. In contrast, electrons in deep traps require extra energy in the form of either

optical or thermal stimulation to migrate to Tb^{3+} emitters. Trapped holes can also migrate toward Tb^{3+} emitters, forming hole-Tb^{3+} centers that radiatively recombine with captured electrons. Notably, electronic calculations of defective $NaLuF_4$ compounds reveal that Eu^{3+} emitters cannot capture hole carriers for afterglow luminescence because the highest occupied 4f level of Eu^{3+} locates in the valence band (Fig. 3b). We measured thermally stimulated luminescence spectra of $NaLuF_4$:Tb nanocrystals in the temperature range of 170 to 470 K (Fig. 3c; Extended Data Fig. 9), and the energy distribution of electron trap states was calculated as 0.12-0.98 eV below the conduction band (Extended Data Fig. 10). By optically stimulating stored electrons to escape from deep traps, we confirmed that high-energy photons produce stronger persistent luminescence compared to low-energy photons (Fig. 3d). The local electronic structure of Tb^{3+} was examined by X-ray absorption near-edge spectroscopy, revealing that Tb^{3+} activators in $NaLuF_4$ nanocrystals maintain a trivalent state (Fig. 3e; Extended Data Fig. 11). Nanoscintillators exhibited high recyclability and photostability under X-ray irradiation and heating at 80 ºC for 14 cycles (Extended Data Fig. 10; Supplementary Movie 1).

The ability to trap X-ray energy in nanoscintillators for persistent radioluminescence prompted us to develop a flexible X-ray detector capable of maintaining images more than 15 days (Fig. 4a; Extended Data Fig. 12). This detector was fabricated by embedding $NaLuF_4$:Tb(15 mol%)@$NaYF_4$ nanoscintillators (2 wt.%) into a polydimethylsiloxane (PDMS) substrate (16 cm × 16 cm × 0.1 cm). Internal structures of a highly curved electronic circuit board can be visualized using the as-fabricated X-ray detector and a digital camera or smartphone (Fig. 4b). High-resolution 3D X-ray imaging was achieved by combining afterglow luminescence and graphical simulations (Supplementary Movie 2). For comparison, only overlapped images of the electronic circuit board were rendered using a typical flat-panel X-ray detector (Fig. 4c; Extended Data Fig. 13). Using thin films containing 2.5 wt% $NaLuF_4$:Tb(15 mol%)@$NaYF_4$ nanoparticles, the X-ray exposure for digital radiography was shortened to one second (Extended Data Fig. 14). We further demonstrated high-resolution X-ray extension microscopy using a highly stretchable detector comprising $NaLuF_4$:Tb@$NaYF_4$ nanoscintillators and commercial silicone rubber (Fig. 4d; Extended Data Fig. 15). The stretchable X-ray detector enabled a spatial imaging resolution of > 20 line pair/mm (< 25 μm), which is significantly higher than that achievable by conventional flat-panel X-ray detectors (typically < 5.0 line pair/mm) (Figs. 4e & 4f; Supplementary Movie 3).

The fundamental advance reported in the Xr-LEI study enables a better understanding of the microscopic mechanism governing long-lived X-ray energy trapping in condensed matter systems such as lanthanide-doped nanocrystals. Our experimental investigations on X-ray-induced generation of Frenkel pair-based trap states offer an entirely new opportunity to fabricate persistent luminescent nanocrystals, which are highly desirable for applications in optogenetics, low-dose radiotherapy[29], optoelectronics[30], expansion microscopy[31], and quantification of radioactive particles such as alpha, beta or high energy gamma. When coupled with highly stretchable elastomers[1, 32-33], these optical nanomaterials may allow the development of next-generation X-ray imaging technologies with unprecedented spatial resolution and special imaging capability for 3D conformal electronics[34-36]. Such low-cost, smartphone-recordable, X-ray imaging techniques are particularly suitable for point-of-care radiography, screening mammogram without breast compression[37], and semiconductor non-destructive inspection.

Online Content Methods, along with any additional Extended Data display items and Source Data, are available in the online version of the paper; references unique to these sections appear only in the online paper.

References

1. J. A. Rogers, T. Someya & Y. Huang, Materials and Mechanics for Stretchable Electronics. *Science 327*, 1603-1607 (2010).
2. S. Wang, et al., Skin electronics from scalable fabrication of an intrinsically stretchable transistor array. *Nature 555*, 83-88 (2018).
3. S. Blahuta, A. Bessiere, D. Gourier, V. Ouspenski & B. Viana, Effect of the X-ray dose on the luminescence properties of Ce:LYSO and co-doped Ca,Ce:LYSO single crystals for scintillation applications. *Opt. Mater. 35*, 1865-1868 (2013).
4. Q. Chen *et al.*, All-inorganic perovskite nanocrystal scintillators. *Nature 561,* 88-83 (2018).
5. S. Yakunin *et al.*, Detection of X-ray photons by solution-processed organic-inorganic perovskites. *Nat. Photonics 9*, 444-449 (2015).
6. H. Wei *et al.*, Sensitive X-ray detectors made of methylammonium lead tribromide perovskite single crystals. *Nat. Photonics 10*, 333-339 (2016).
7. W. Wei *et al.*, Monolithic integration of hybrid perovskite single crystals with heterogenous substrate for highly sensitive X-ray imaging. *Nat. Photonics 11*, 315-321 (2017).
8. P. Büchele *et al.*, X-ray imaging with scintillator-sensitized hybrid organic photodetectors. *Nat. Photonics 9*, 843-848 (2015).
9. Q. I. M. de Chermont *et al.*, Nanoprobes with near-infrared persistent luminescence for in vivo

imaging. *Proc. Natl. Acad. Sci. U. S. A.* **104**, 9266-9271 (2007).

10. T. Maldiney *et al.*, The in vivo activation of persistent nanophosphors for optical imaging of vascularization, tumours and grafted cells. *Nat. Mater.* **13**, 418-426 (2014).

11. T. Matsuzawa, Y. Aoki, N. Takeuchi & Y. Murayama, A New Long Phosphorescent Phosphor with High Brightness, $SrAl_2O_4:Eu^{2+},Dy^{3+}$. *J. Electrochem. Soc.* **143**, 2670-2673 (1996).

12. Z. Pan *et al.*, Sunlight-activated long-persistent luminescence in the near-infrared from Cr^{3+}-doped zinc gallogermanates. *Nat. Mater.* **11**, 58-63 (2011).

13. Z. Xue *et al.*, X-ray-activated Near-infrared persistent luminescent probe for deep-tissue and renewable in vivo bioimaging. *ACS Appl. Mater. Interfaces* **9**, 22132-22142 (2017).

14. L. Song *et al.*, Low-Dose X-ray Activation of W(VI)-Doped Persistent Luminescence Nanoparticles for Deep-Tissue Photodynamic Therapy. *Adv. Funct. Mater.* **28,** 1707496 (2018).

15. Y. Li *et al.*, Long persistent phosphors-from fundamentals to applications. *Chem. Soc. Rev.* **45**, 2090-2136 (2016).

16. A. Shyichuk *et al.*, Energy transfer upconversion dynamics in $YVO_4:Yb^{3+},Er^{3+}$. *J. Lumin.* **170**, 560-570 (2016).

17. J. A. Capobianco, F. Vetrone, J. C. Boyer, A. Speghini & M. Bettinelli, Enhancement of red emission ($^4F_{9/2}{\rightarrow}^4I_{15/2}$) via upconversion in bulk and nanocrystalline cubic $Y_2O_3:Er^{3+}$. *J. Phys. Chem. B* **106**, 1181-1187 (2002).

18. E. Zych, C. Brecher, A. J. Wojtowicz & H. Lingertat, Luminescence properties of Ce-activated YAG optical ceramic scintillator materials. *J. Lumin.* **75**, 193-203 (1997).

19. S. Kurosawa, Y. Yokota, T. Yanagida, A. Yoshikawa, Eu-concentration dependence of optical and scintillation properties for Eu-doped SrF_2 single crystals. *Phys. Status Solidi C* **9**, 2275-2278 (2012).

20. M. Nikl, A. Yoshikawa, Recent R&D Trends in Inorganic Single-Crystal Scintillator Materials for Radiation Detection. *Adv. Opt. Mater.* **3**, 463-481 (2015).

21. Y. Liu *et al.*, Amplified stimulated emission in upconversion nanoparticles for super-resolution nanoscopy. *Nature* **543**, 229-233 (2017).

22. M. B. Prigozhin *et al.*, Bright sub-20-nm cathodoluminescent nanoprobes for electron microscopy. *Nat. Nanotechnol.* **14**, 420-425 (2019).

23. J. C. G. Bunzli, Lanthanide luminescence for biomedical analyses and imaging. *Chem. Rev.* **110**, 2729-2755 (2010).

24. A. Fernandez-Bravo *et al.*, Continuous-wave upconverting nanoparticle microlasers. *Nat. Nanotechnol.* **13**, 572-577 (2018).

25. C. B. Lushchik, Creation of Frenkel defect pairs by excitons in alkali halides. *Modern Problems in Condensed Matter Sciences*, Elsevier. **13**, 473-525 (1986).

26. M. J. Berger *et al.*, https://www.nist.gov/pml/xcom-photon-cross-sections- database. *XCOM: Photon Cross Sections Database* (2013).

27. D. R. Cooper, J. A. Capobianco & J. Seuntjens, Radioluminescence studies of colloidal oleate-capped beta-Na(Gd, Lu)$F_4:Ln^{3+}$ nanoparticles (Ln = Ce, Eu, Tb). *Nanoscale* **10**, 7821-7832 (2018).

28. M. Kang *et al.*, Resolving the nature of electronic excitations in resonant inelastic X-ray scattering. *Phys. Rev. B* **99**, 045105 (2019).

29. K. Lu *et al.*, Low-dose X-ray radiotherapy–radiodynamic therapy via nanoscale metal–organic frameworks enhances checkpoint blockade immunotherapy. *Nat. Biomed. Eng.* **2,** 600-610 (2018).

30. Y. Yang *et al.*, X-ray-activated long persistent phosphors featuring strong UVC afterglow

emissions. *Light Sci. Appl. 7*, 88 (2018).

31. F. Chen, P. W. Tillberg & E. S. Boyden, Expansion microscopy. *Science 347*, 543-548 (2015).
32. J. Y. Sun *et al.*, Highly stretchable and tough hydrogels. *Nature 489*, 133-136 (2012).
33. C. Li *et al.*, A highly stretchable autonomous self-healing elastomer. *Nat. Chem. 8*, 619-625 (2016).
34. B. A. Palmer *et al.*, X-ray birefringence imaging. *Science 344*, 1013-1016 (2014).
35. P. Thibault *et al.*, High-Resolution Scanning X-ray Diffraction Microscopy. *Science 321*, 379-382 (2008).
36. M. Holler *et al.*, High-resolution non-destructive three-dimensional imaging of integrated circuits. *Nature 543,* 402-406 (2017).
37. W. Zhao, J. A. Rowlands, X-ray imaging using amorphous selenium: Feasibility of a flat panel self-scanned detector for digital radiology. *Med. Phys. 22*, 1595-1604 (1995).

Author contributions X.O. and H.Y. initiated the project. Q.C. and X.L. conceived the concept of X-ray luminescence extension imaging of 3D electronics. X.L., H.Y. and Q.C. supervised the project and organized the collaboration. X.O., X.L., H.Y. and Q.C. designed experiments. X.O., Q.W., X.C., Z.H. and J.Z. performed nanocrystal synthesis. X.O., Q.W., J.Z. and L.X. performed luminescence measurements and X-ray imaging. X.O., Z.Y., and H.B. performed flexible X-ray imaging. X.Q. and B.H. carried out theoretical calculations. J.L., H.B. and Y.W. fabricated PDMS molds and measured low-temperature scintillation spectra. X.O., H.Y., Q.C., and X.L. wrote the manuscript. All authors discussed the results and commented on the manuscript.

Competing interests The authors declare no competing interests.

Author Information Reprints and permissions information is available online at http://www.nature.com/reprints. The authors declare no competing financial interests. Readers are welcome to comment on the online version of the paper. Correspondence and requests for materials should be addressed to H.Y. (hhyang@fzu.edu.cn), Q.C. (qchen@fzu.edu.cn) or X.L. (chmlx@nus.edu.sg).
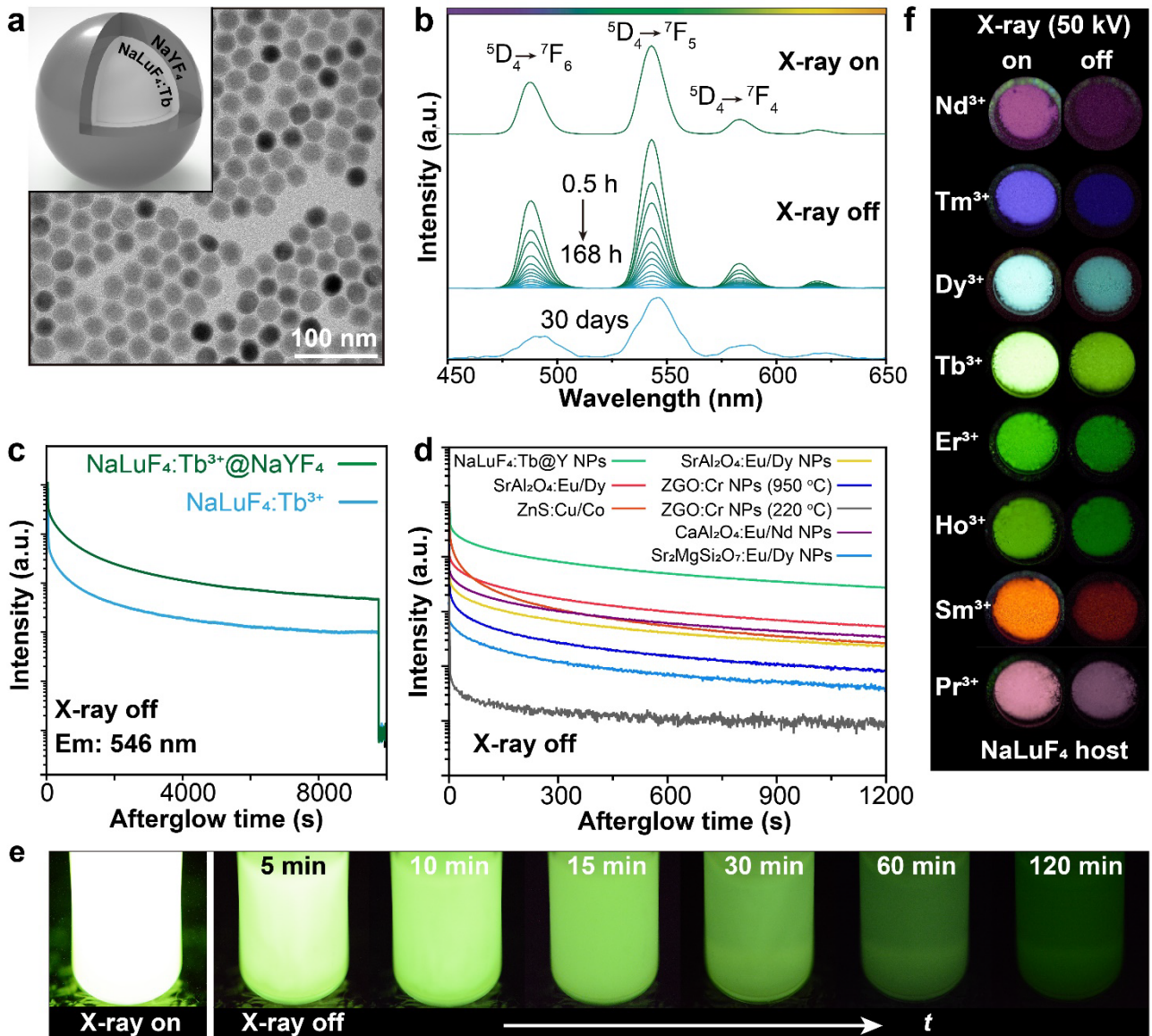
Figure 1 | Characterization of lanthanide-doped persistent luminescent nanoscintillators. a, TEM micrograph of NaLuF$_4$:Tb (15 mol%)@NaYF$_4$ nanocrystals. **b,** Radioluminescent emission spectra of the as-synthesized core-shell nanocrystals, recorded under X-ray excitation at a voltage of 50 kV and upon turning off X-rays for 0.5-168 h and 30 days. **c,** Radioluminescent intensity of NaLuF$_4$:Tb (15 mol%) and NaLuF$_4$:Tb (15 mol%)@NaYF$_4$ nanocrystals, monitored at 546 nm as a function of time upon cessation of X-rays. **d,** Comparison of afterglow decay profiles of various phosphors after ceasing X-ray excitation (50 kV). **e,** Afterglow photographs of NaLuF$_4$:Tb(15 mol%)@NaYF$_4$ nanocrystals dispersed in 1-mL cyclohexane. X-ray operation was set at a voltage of 70 kV and a tube current of 1 mA. **f,** Time-dependent afterglow photographs of NaLuF$_4$ nanocrystals doped with various activators (Nd^{3+}, Tm^{3+}, Dy^{3+}, Tb^{3+}, Er^{3+}, Ho^{3+}, Sm^{3+} and Pr^{3+}).
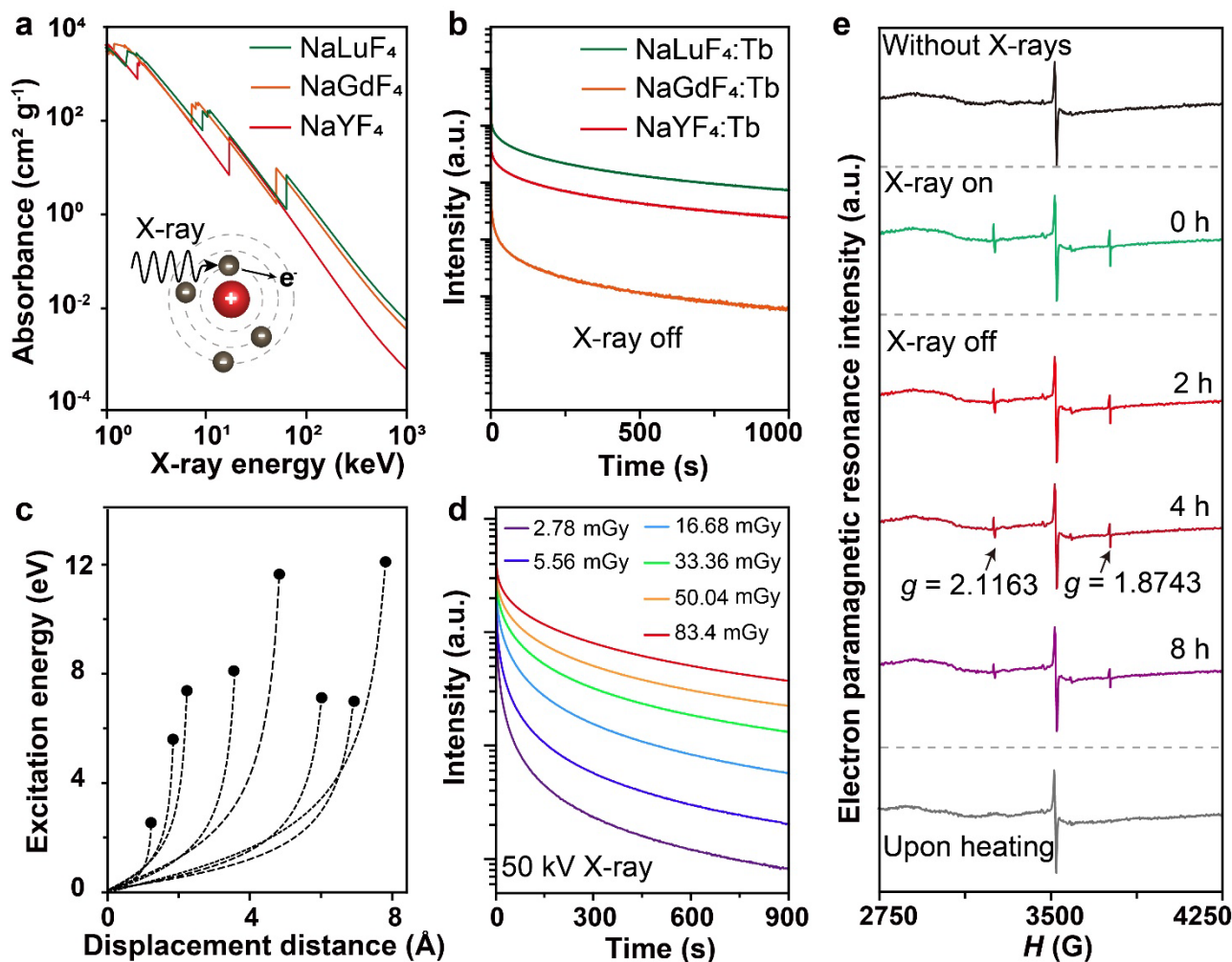
Figure 2 | Photophysical studies of X-ray irradiation on lanthanide-doped nanoscintillators. a, Absorption spectra of $NaYF_4$, $NaGdF_4$ and $NaLuF_4$ as a function of X-ray energy. Attenuation coefficients were obtained from ref *26*. The inset shows X-ray absorption by an atom and the transition of its inner-shell electrons. **b,** Room-temperature radioluminescent afterglow intensity of $NaYF_4$:Tb (15 mol%), $NaGdF_4$:Tb (15 mol%) and $NaLuF_4$:Tb (15 mol%) nanocrystals as a function of time upon removal of X-ray irradiation. All samples were excited with X-ray irradiation at a voltage of 50 kV. **c,** Dependence of transient formation energy on the separation distance between V_F and I_F sub-defects. **d,** Radioluminescent decay curves of the $NaLuF_4$:Tb (15 mol%) nanocrystals after illuminating with different X-ray excitation dosage at room temperature. **e,** Electron paramagnetic resonance (EPR) spectra of the as-synthesized $NaLuF_4$:Tb (15 mol%) nanocrystals. Samples were measured at room temperature under the following conditions: before X-rays, during X-rays, 2, 4, and 8 hours after cessation of X-rays, and after heating at 200 °C, respectively.
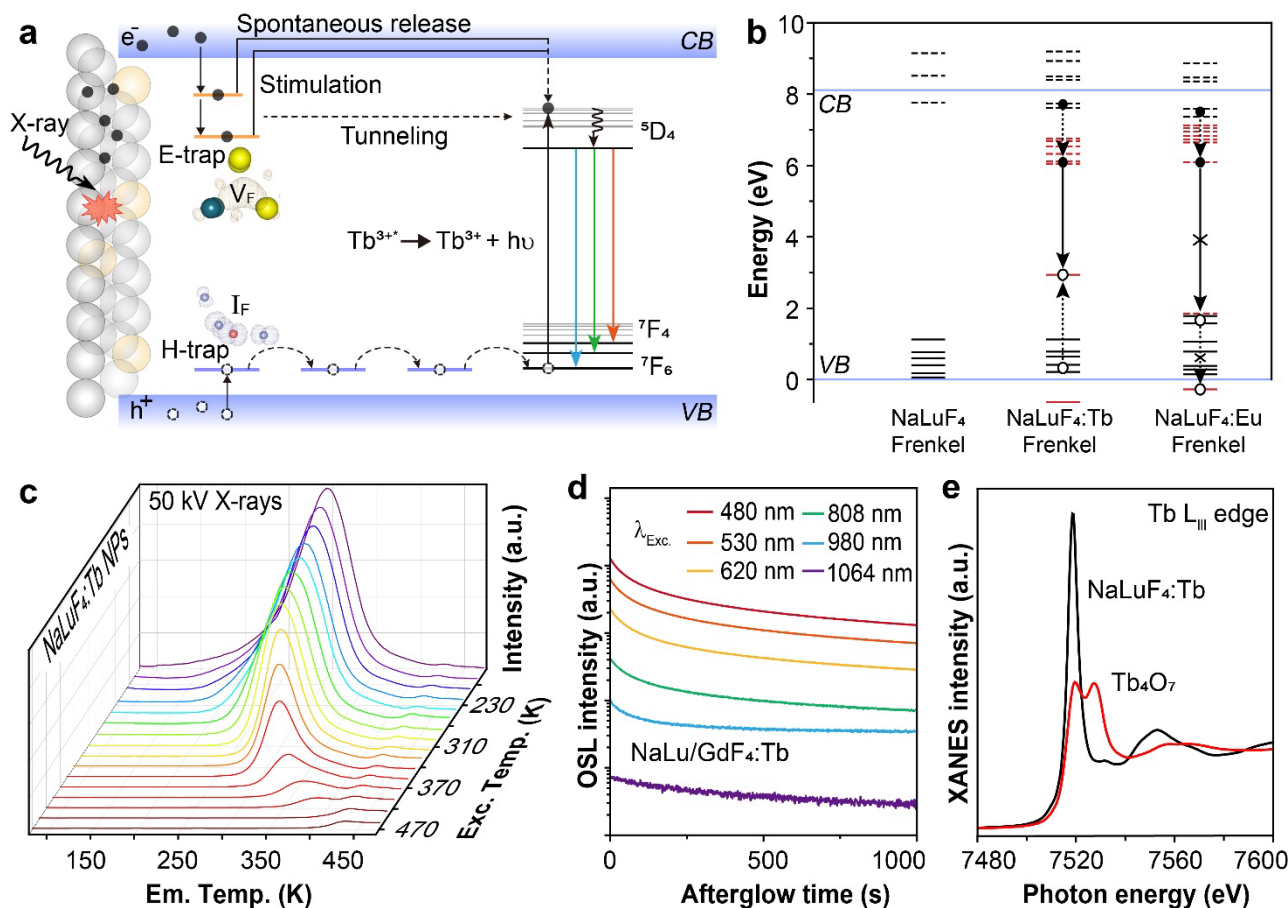
Figure 3 | Mechanistic investigations of X-ray energy trapping in lanthanide-doped nanoscintillators. a, Proposed emission mechanism of long-lived persistent radioluminescence involving Tb^{3+}-doped $NaLuF_4$ nanocrystals. Upon X-ray excitation, electrons at an inner electronic shell of lattice atoms are photoexcited to produce low-energy electrons, which are either transferred to activators for emission or partially stored at electronic trap states. Electrons in shallow traps release slowly for spontaneous long-lasting emission of Tb^{3+}. In contrast, electrons in deep traps populate to the conduction band (CB) under optical or thermal stimulation. **b,** Energy diagram of defective $NaLuF_4$ compounds. Solid and dotted black-lines represent occupied and empty states of defective $NaLuF_4$ compounds. Solid and dotted red-lines denote 4f-related occupied and empty states, respectively. black dots and circles denote trapped electrons and holes. **c,** Thermally-stimulated luminescence spectra of $NaLuF_4$:Tb (15 mol%) nanocrystals measured in the temperature range of 170 to 470 K. The sample was first irradiated by an X-ray source for 300 s. After cessation of the X-ray source for 10 min, emission spectra were measured at a heating rate of 1 K/s. **d,** Optically stimulated luminescence decay profiles of $NaLuF_4$:Tb/Gd (15/5 mol%) nanocrystals, recorded upon turning off X-rays and photostimulation at 480, 530, 620, 808, 980, and 1064 nm for 2 min, respectively. All measurements were performed at room temperature one hour after luminescence afterglow of the samples faded. **e,** X-ray absorption near edge structure (XANES) spectra of Tb L_{III} edge recorded for $NaLuF_4$:Tb (15 mol%) nanocrystals and a Tb_4O_7 reference sample.
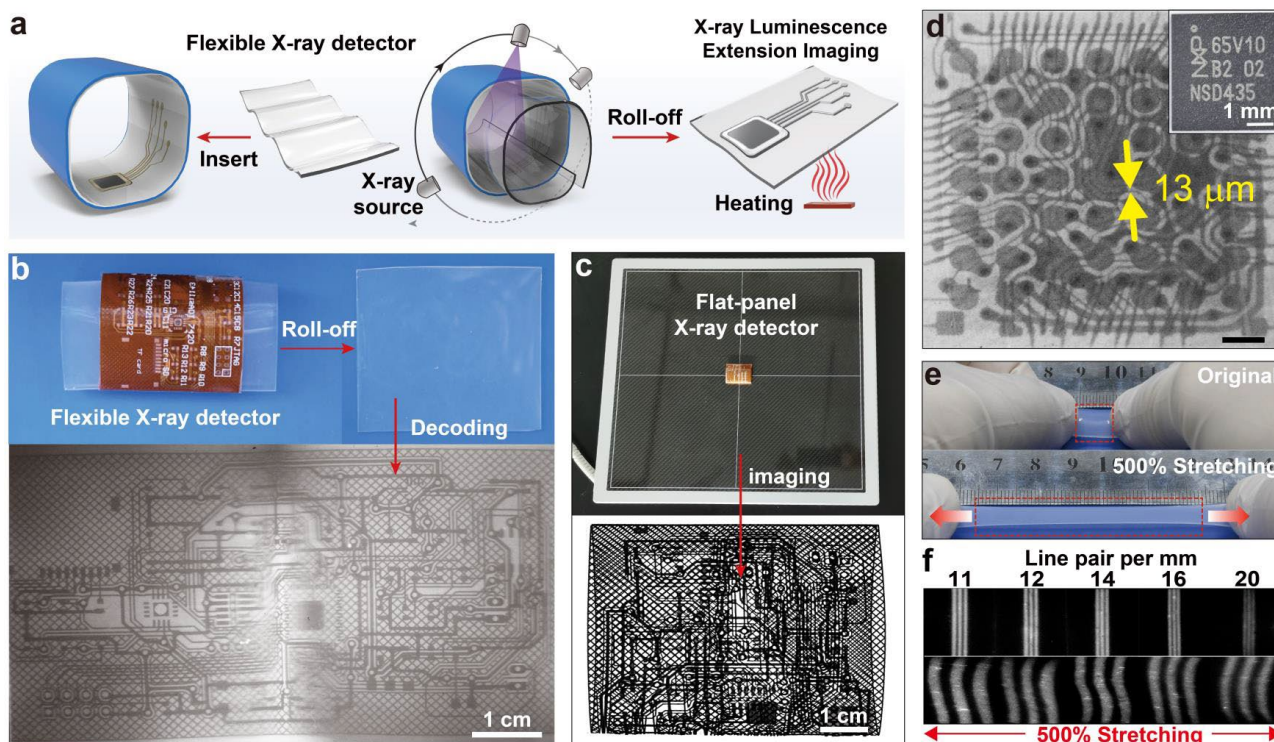
Figure 4 | High-resolution X-ray luminescence extension imaging (Xr-LEI). a, Schematic showing 3D electronic imaging enabled by a nanoscintillator-integrated, flexible X-ray detector. First, the detector is inserted into a 3D electronic circuit board so as to conform to it. Next, the image of the electronic board is projected onto the X-ray detector. Upon stoppage of X-rays, the detector can be transferred on a hot substrate for microscopy imaging under thermal stimulation. **b,** Xr-LEI of a 3D electronic board using a prototype, NaLuF$_4$:Tb@NaYF$_4$-based X-ray detector (X-ray voltage, 50 kV; heating temperature, 80 °C). **c,** X-ray imaging of the same circuit board using a conventional flat-panel X-ray detector. **d,** Xr-LEI of integrated circuits inside an iPhone 6 Plus smartphone (voltage, 50 kV; scale bar, 500 μm). The insert is the corresponding digital photograph of the circuits. **e,** Photograph of a stretchable, NaLuF$_4$:Tb@NaYF$_4$-based X-ray detector. **f,** Characterization of X-ray imaging resolution using the stretchable X-ray detector (voltage, 50 kV).

Methods

Chemicals. Gadolinium (III) acetate hydrate (Gd(CH$_3$CO$_2$)$_3$•xH$_2$O, 99.9%), yttrium (III) acetate hydrate (Y(CH$_3$CO$_2$)$_3$•xH$_2$O, 99.9%), lutetium (III) acetate hydrate (Lu(CH$_3$CO$_2$)$_3$•xH$_2$O, 99.9%), thulium (III) acetate hydrate (Tm(CH$_3$CO$_2$)$_3$•xH$_2$O, 99.9%), praseodymium (III) chloride hydrate (PrCl$_3$•xH$_2$O, 99.9%), neodymium (III) acetate hydrate (Nd(CH$_3$CO$_2$)$_3$•xH$_2$O, 99.9%), samarium (III) acetate hydrate (Sm(CH$_3$CO$_2$)$_3$•xH$_2$O, 99.9%), terbium (III) acetate hydrate (Tb(CH$_3$CO$_2$)$_3$•xH$_2$O, 99.9%), dysprosium (III) acetate hydrate (Dy(CH$_3$CO$_2$)$_3$•xH$_2$O, 99.9%), holmium (III) acetate hydrate (Ho(CH$_3$CO$_2$)$_3$•xH$_2$O, 99.9%), erbium (III) acetate hydrate (Er(CH$_3$CO$_2$)$_3$•xH$_2$O, 99.9%), zinc nitrate hexahydrate (Zn(NO$_3$)$_2$•6H$_2$O, >99%), gallium (III) nitrate hydrate (Ga(NO$_3$)$_3$•xH$_2$O, 99.9%), chromium (III) nitrate nonahydrate (Cr(NO$_3$)$_3$•9H$_2$O, 99%), sodium hydroxide (NaOH, >98%), ammonium fluoride (NH$_4$F, >98%), 1-octadecene (ODE, 90%), oleic acid (OA, 90%), and cyclohexane (chromatography grade, 99.7%) were purchased from Sigma-Aldrich. SYLGARD^{TM} 184 silicone elastomer kit was purchased from Dow Corning. Persistent phosphor powders of CaAl$_2$O$_4$:Eu^{2+}/Nd^{3+}, Sr$_2$MgSi$_2$O$_7$:Eu^{2+}/Dy^{3+}, SrAl$_2$O$_4$:Eu^{2+}/Dy^{3+} and ZnS:Cu^{2+}/Co^{2+} were purchased from Xiucai Chemical Co., Ltd. (Foshan, China). Type-38 and Type-74 line pair charts were purchased from Hua Ruisen Technology Development Co., Ltd. (Beijing, China). Tb$_4$O$_7$ powder was purchased from Aladdin Biochemical Technology Co., Ltd. (Shanghai, China). BC422 plastic scintillator was a mixture of PVT and small molecules of 2-(4-*tert*-butylphenl)-5-(4-biphenylyl)-1,3,4-oxadiazole, obtained from Saint-Gobain (USA). ST401 plastic scintillator was purchased from Zhonghelixin Co., Ltd (Chengdu, China). Unless otherwise noted, all chemicals were used without further purification.

Synthesis of β-NaLuF$_4$:Ln/Gd (x/(20-x) mol%) nanocrystals. Oleic acid-capped NaLuF$_4$:Ln/Gd (x/(20-x) mol%) (Ln^{3+} = Pr^{3+}, Nd^{3+}, Sm^{3+}, Tb^{3+}, Dy^{3+}, Ho^{3+}, Er^{3+} & Tm^{3+}; x = 0.5-15) nanocrystals were synthesized using a coprecipitation method[22]. In a typical experiment, a mixture of Ln(CH$_3$CO$_2$)$_3$ •xH$_2$O (0.5 mmol; Ln = Lu, Gd, Tb, Nd, Sm, Dy, Ho, Er & Tm) or PrCl$_3$•xH$_2$O in the desired ratio was added into a 50-mL two-necks round-bottom flask containing 5 mL of OA and 7.5 mL of ODE. The mixture was heated to 150 °C under vacuum for 30 min. After cooling to room temperature, 10 mL of methanol containing 2 mmol NH$_4$F and 1.25 mmol NaOH were added to the solution. The resulting solution was vigorously stirred at 50 °C for 30 min, followed by heating at 100 °C under vacuum for another 10 min. The reaction mixture was quickly heated to 300 °C at a rate of 20 °C/min for 1 h under a nitrogen atmosphere with stirring. After cooling to room temperature, the resultant nanocrystals were precipitated by addition of ethanol, collected by 8000 rpm centrifugation for 5 min, washed with absolute ethanol, dispersed in 4 mL of cyclohexane, and finally stored in a freezer at 4 °C.

Synthesis of β-NaLuF$_4$:Tb/Gd (15/x mol%) nanocrystals. The synthetic procedure for NaLuF$_4$:Tb^{3+}/Gd^{3+} (15/x mol%; x = 0-35) nanocrystals was identical to the synthesis of NaLuF$_4$:Tb^{3+}/Gd^{3+} (x/(20-x) mol%; x = 2-20) nanocrystals.

Synthesis of β-NaReF$_4$:Tb (15 mol%) nanocrystals. The synthetic procedure for NaReF$_4$:Tb (15 mol%) (Re = Y or Gd) nanocrystals was identical to the synthesis of NaLuF$_4$:Tb (15 mol%)

nanocrystals except for heating temperature and heating duration. To a 50-mL round-bottom two-necks flask, 5 mL of OA and 7.5 mL of ODE were added with a total amount of 0.5 mmol $Re(CH_3CO_2) \cdot xH_2O$ (Re = Y, Gd, & Tb). The resulting solution was heated at 150 ˚C for 30 min under stirring and then cooled to room temperature. Afterward, a methanol solution (10 mL) containing NH_4F (2 mmol) and NaOH (1.25 mmol) was added to the solution. This solution was heated at 50 ˚C for 30 min under stirring. Upon removal of methanol by heating at 100 ˚C for 10 min, the resulting solution was kept at 295 ˚C for 1.5 h. Products were precipitated with ethanol, collected by centrifugation at 8000 rpm for 10 min, washed with absolute ethanol, and finally dispersed in 4 mL cyclohexane.

Synthesis of β-NaLuF₄:Tb@NaYF₄ core-shell nanocrystals. The β-NaLuF₄:Tb@NaYF₄ core-shell nanocrystals were prepared using an epitaxial growth method. In a typical experiment, 0.5 mmol $Y(CH_3COO) \cdot 4H_2O$ in 4 mL of OA and 16 mL of ODE were heated to 150 ºC under vacuum for 30 min and then cooled to room temperature. The temperature was then decreased to 50 ºC, and 4 mL of as-prepared core nanocrystals were added to the mixture and heated at 80 ºC for 10 min to evaporate cyclohexane. After cooling to room temperature, a solution of 2 mmol NH_4F and 1.25 mmol NaOH dissolved in 10 mL of methanol was added. The resulting mixture was vigorously stirred at 50 ºC for 30 min and then heated at 100 ºC for 10 min. The reaction mixture was then quickly heated to 295 ºC for 1.5 h under a nitrogen atmosphere while stirring. After cooling to room temperature, the resulting core-shell nanocrystals were precipitated by addition of ethanol, collected by centrifugation, washed with absolute ethanol, and dispersed in 4-mL cyclohexane.

Synthesis of β-NaGdF₄:Tb@NaYF₄ core-shell nanocrystals. The synthetic procedure for NaGdF₄:Tb@NaYF₄ nanocrystals was identical to the synthesis of NaLuF₄:Tb@NaYF₄ nanocrystals.

Synthesis of β-NaGdF₄:Eu nanocrystals. The synthetic procedure for NaGdF₄:Eu (15 mol%) nanocrystals was identical to the synthesis of NaGdF₄:Tb (15 mol%) nanocrystals.

Preparation of ZnGa₁.₉₉₅O₄:Cr₀.₀₀₅ persistent luminescence nanoparticles. In a typical procedure, persistent luminescence nanoparticles were prepared by a hydrothermal method, followed by sintering in an inert atmosphere. A solution of $Zn(NO_3)_2 \cdot 6H_2O$ (0.2668 g, 0.897 mmol), $Ga(NO_3)_3 \cdot xH_2O$ (0.4577 g, 1.7895 mmol), and $Cr(NO_3)_3 \cdot 9H_2O$ (0.0018 g, 0.0045 mmol) was added to a round-bottom flask and vigorously stirred at room temperature. The total volume was adjusted to 16 mL by adding ultrapure water. Then, ammonium hydroxide (28 wt%) solution was quickly added to adjust the pH to ~ 6.5 while a white precipitate gradually formed. After stirring for 30 min, the mixture was transferred to a Teflon-lined autoclave (25 mL). The autoclave was put in an oven at 220 °C. After 12 h reaction, the system was cooled to room temperature. The resulting products were washed with deionized water three times to remove excess inorganic species and subsequently dried at 60 °C overnight. The powder was further sintered in air at 950 °C for 4 h.

Physical characterization. Transmission electron microscopy and high-resolution transmission electron microscopy (HR-TEM) images were taken on a Tecnai G2 F20 S-TWIN microscope (FEI Nano Ports, USA) operated at an accelerating voltage of 200 kV. Elemental mapping analysis was performed using a scanning transmission electron microscopy and energy-dispersive X-ray

spectroscopy (STEM-EDS) equipped with a Tecnai G2 F20 S-TWIN microscope at an accelerating voltage of 120 kV. High-resolution STEM characterization was done with an FEI aberration-corrected Titan Cubed S-Twin transmission electron microscope at an accelerating voltage of 60 kV. Scanning electron microscope characterization was performed on a Verios G4 XHR electron microscope (Thermal Fisher Scientific, USA). Radioluminescent spectra and persistent luminescence decay curves were measured using an Edinburgh FS5 fluorescence spectrophotometer (Edinburgh Instruments Ltd, U.K.) equipped with a miniature X-ray source (Amptek, Inc., USA). Thermally-stimulated luminescence was measured using an Edinburgh FS5 spectrophotometer coupled with an HFS 600 heating/cooling stage (Linkam Scientific Instruments Ltd, UK) and a customized optical fiber. XRD patterns were obtained using an X-ray powder diffractometer (D/MAX-3C, Rigaku Co., Japan) over the angular range of 5-90°. Photographs of X-ray-induced luminescence and radioluminescence-based X-ray imaging were acquired with a digital camera (Nikon, D850 coupled with AF-S Micro-Nikkor 105 mm 2.8G or AF-S Micro-Nikkor 40 mm 2.8G) in an all-manual mode. Electron paramagnetic resonance (EPR) was carried out using a Bruker model A300 spectrometer recorded at 9.85GHz (Bruker Co., USA). X-ray absorption fine structure spectra were collected with a BL14W beamline at the Shanghai Synchrotron Radiation Facility (SSRF). Storage rings of SSRF were operated at 3.5 GeV with a stable current of 200 mA. Using Si (111) double-crystal monochromator, data collection was carried out in fluorescence mode using a Lytle detector. All spectra were collected under ambient conditions.

Mechanical compression of persistent phosphors. Persistent phosphors were poured into an open mould (diameter, 7 mm). A pressure of 2 tons was applied to compress the powder for 20 s. A round disc of the powder was removed from the open mould for further characterization. The open mould and tablet machine were purchased from Jingtuo Instrument and Technology Co., Ltd (Tianjin, China).

Electronic trap depth of NaLuF$_4$:Tb/Gd (15/x mol%; x = 0-35) nanocrystals. The depth of electronic traps was characterized by measuring temperature-dependent thermoluminescence spectra of the NaLuF$_4$:Tb/Gd (15/x mol%; x = 0-35) nanocrystals using the initial rise analysis method[38]. In a typical procedure, materials were heated at a temperature of 550 K to completely release their trapped carriers using a cooling/heating stage (Linkam Scientific Instruments Ltd, HSF 600, UK). Next, these samples were excited by an X-ray source for 5 min at a set temperature. Afterward, samples were heated to 550 K at a rate of 1 K/s. Light output was measured using an Edinburgh FS5 spectrometer coupled with an optical fiber.

Mechanical characterization. The stretchability of silicone rubber was measured with an electrical universal material testing machine (CMT4104, MTS Systems Co, Ltd., China). Silicone rubber samples were cut into rectangles 50 mm in length, 10 mm in width, and 1 mm in thickness.

Fabrication of a flexible X-ray detector. In a typical experiment, SYLGARD^{TM} 184 silicone elastomer base was premixed with the curing agent (10:1 by mass). Platinum-catalyzed rubber elastomer was prepared by casting the commercial Ecoflex 30 (Smooth-On) mixture (Part A and Part B in 1:1 weight ratio). A cyclohexane solution of NaLuF$_4$:Tb(15 mol%)@NaYF$_4$ nanocrystals with various concentrations was added to the resultant solution and stirred vigorously. Resultant

mixture was poured into a square acrylic plate (16×16 cm^2) as a mold for thin-film fabrication. The resulting composites were degassed in a vacuum container to remove air bubbles. The mixture was finally heated at 80 °C for 4 hours. After cooling to room temperature, the as-fabricated film (thickness: 1 mm) was peeled from the square acrylic template and used for X-ray imaging.

Experimental setup for X-ray luminescence extension imaging. A CCD camera (Tucsen, FL-20BW) was coupled with AZURE-6515TH10M objective (AZURE Photonics Co., Ltd., China) and fixed on a bracket (Olympus China Co., Ltd.) using a quasi-focus screw. A heating plate was placed under the flexible X-ray detector to stimulate radioluminescence afterglow after turning off X-rays.

Digital X-ray imaging. In a typical procedure for X-ray imaging, the flexible X-ray detector was inserted into an electronic board or placed on its surface. A beam of X-ray source (P357, VJ Technologies Co, Ltd. (Suzhou, China)) or miniature X-ray source (Amptek, Inc., USA) was applied to the electronic board with different amounts of X-ray exposure. After X-ray exposure, the flexible X-ray detector was placed on a metal plate and heated to 80 °C. Images were recorded using a digital camera (exposure time, 10 s) or a smartphone or an optical microscope.

3D modelling for X-ray imaging. The 3D model for X-ray imaging of a printed circuit board was constructed using Solidworks software. X-ray images obtained through luminescence afterglow were pasted on the surface of constructed object model.

Calculation of electronic trap depth using the initial rise analysis method. Thermally-stimulated luminescence was performed to investigate the electronic trap depth in the as-synthesized persistent luminescent nanomaterials. Using the initial analysis method, temperature-dependent luminescence spectra under different excitation temperatures were measured to calculate the distribution of trap depth. The equation for the first, second, and general order afterglow curve can be expressed as:

$$I(T) = C \exp\left(-\frac{E_t}{kT}\right) \ (1)$$

Where I is the intensity of thermally-stimulated luminescence, C is a constant, E_t is the defect energy level, k is Boltzmann constant, and T is the temperature. When the equation was plotted in an Arrhenius kinetic process, the equation in (1) can be expressed as:

$$\ln I(T) = \ln C - \frac{E_t}{kT} \ (2)$$

Hence, the trap depth can be determined by the slope of the straight section on the low-temperature side:

$$E_t = -k \times 8.617 \times 10^{-2} \ eV \ (3)$$

The glow curves of equation (1) are integrated to obtain the density of trapped electrons. The distribution of trap depth can be obtained by calculating the difference between each energy level.

Density functional theory. Density functional theory (DFT) calculations were performed to determine the ground-state electronic properties of both intrinsic and Tb-doped NaLuF$_4$ lattice with P6$^-$ space group. To correct the on-site Coulomb energy of the spurious electron self-energy, we introduced a self-consistent determined U parameter on the localized $4f$ orbitals of rare earth

elements. DFT+U calculations were conducted using the CASTEP (Cambridge Serial Total Energy Package) source code[39], and the norm-conserving pseudopotentials for Na, Tb, Lu and F atoms were generated using the OPIUM code in the Kleinman-Bylander projector form [40]. Note that nonlinear partial core correction and a scalar relativistic averaging scheme are used to treat the spin-orbital coupling effect [41]. In particular, we treated the (4f, 5s, 5p, 5d, 6s) states as valence states of the Tb and Lu atoms. For all the calculations of electronic structures, to correct the on-site Coulomb energy of the electron spurious self-energy, we have applied the self-consistent determination for the U correction on the localized 4f orbitals. In particular for the semicore d or f orbitals in heavy elements with mixed valences, we established a manner to determine the on-site electronic self-energy and related wave function relaxation for obtaining accurate orbital eigenvalues of the electronic structures and transition levels[42]. We have chosen the ab initio two-way crossover searching calculation by using two different functionally compiled CASTEP-17 developing source codes[43-44].

The time-dependent density functional theory (TD-DFT) calculation is then performed with a two-electron-based Tamm-Dancoff approximation imported from our self-consistent corrected ground-state wave functio[45]. By calculating excitation energies and transition probabilities, one could theoretically retrieve a full set of optical properties of systems under study, which are able to reveal more accurate locations of absorption peaks in the optical spectrum than Kohn-Sham excitation energies[45].

Finite element simulation. To investigate tensile strain (the first principal stress) on the silicone rubber film structure, the finite element simulations were performed using commercial FET software COMSOL (COMSOL LIC, Sweden). Geometries were meshed using eight-node hexahedron elements. The Mooney-Rivlin model was used to capture the hyperelastic behavior of the material. For the random point in elastomer, the equilibrium differential equation along the Cartesian axis (x, y, z) can be expressed as:

$$
\begin{cases}
\dfrac{\partial \sigma_x}{\partial x} + \dfrac{\partial \tau_{xy}}{\partial y} + \dfrac{\partial \sigma_{xz}}{\partial z} + f_x = 0 \\[2mm]
\dfrac{\partial \tau_{yx}}{\partial x} + \dfrac{\partial \sigma_y}{\partial y} + \dfrac{\partial \tau_{yz}}{\partial z} + f_y = 0 \\[2mm]
\dfrac{\partial \tau_{zx}}{\partial x} + \dfrac{\partial \tau_{yz}}{\partial y} + \dfrac{\partial \sigma_z}{\partial z} + f_z = 0
\end{cases}
$$

Where f_x, f_y, and f_z are the components of the vector of the stress per unit volume in the x, y, and z directions. When slight displacement and deformation occur, if higher-order and nonlinear terms of the displacement derivative are omitted, the geometric equation in the Cartesian coordinate system x, y, z can be expressed as:

$$
\begin{cases}
\varepsilon_x = \dfrac{\partial u}{\partial x}, \gamma_{xy} = \dfrac{\partial u}{\partial y} + \dfrac{\partial v}{\partial x} \\[2mm]
\varepsilon_y = \dfrac{\partial v}{\partial y}, \gamma_{yz} = \dfrac{\partial v}{\partial z} + \dfrac{\partial w}{\partial y} \\[2mm]
\varepsilon_z = \dfrac{\partial w}{\partial z}, \gamma_{xz} = \dfrac{\partial u}{\partial z} + \dfrac{\partial w}{\partial x}
\end{cases}
$$

When large displacement and deformation occur, nonlinear terms of displacement derivatives are preserved, and the geometric equation in the Cartesian coordinate system x, y, z can be expressed as:

$$
\begin{cases}
\varepsilon_x = \dfrac{\partial u}{\partial x} + \dfrac{1}{2}\left[\left(\dfrac{\partial u}{\partial x}\right)^2 + \left(\dfrac{\partial v}{\partial x}\right)^2\right], \gamma_{xy} = \dfrac{\partial v}{\partial x} + \dfrac{\partial u}{\partial y} + \dfrac{\partial u}{\partial x}\dfrac{\partial u}{\partial y} + \dfrac{\partial v}{\partial x}\dfrac{\partial v}{\partial y} \\[2mm]
\varepsilon_y = \dfrac{\partial v}{\partial y} + \dfrac{1}{2}\left[\left(\dfrac{\partial v}{\partial y}\right)^2 + \left(\dfrac{\partial w}{\partial y}\right)^2\right], \gamma_{yz} = \dfrac{\partial v}{\partial z} + \dfrac{\partial w}{\partial y} + \dfrac{\partial v}{\partial y}\dfrac{\partial v}{\partial z} + \dfrac{\partial w}{\partial y}\dfrac{\partial w}{\partial z} \\[2mm]
\varepsilon_z = \dfrac{\partial w}{\partial z} + \dfrac{1}{2}\left[\left(\dfrac{\partial w}{\partial z}\right)^2 + \left(\dfrac{\partial u}{\partial z}\right)^2\right], \gamma_{xz} = \dfrac{\partial u}{\partial z} + \dfrac{\partial w}{\partial x} + \dfrac{\partial w}{\partial z}\dfrac{\partial w}{\partial x} + \dfrac{\partial u}{\partial z}\dfrac{\partial u}{\partial x}
\end{cases}
$$

The physical equation can be expressed as:

$$\sigma = K^T \sigma_I = K^T D_I \varepsilon_I = K^T D_I K \varepsilon = D\varepsilon$$

Where D is an elastic matrix.

Supposing that the internal force per unit area of the elastic body on the boundary is T_x, T_y, T_z, and the area force acting on the unit area of the known elastomer on the boundary $S\sigma$ is $\overline{T}_x, \overline{T}_y, \overline{T}_z$. According to the plane conditions:

$$T_x = \overline{T}_x, T_y = \overline{T}_y, T_z = \overline{T}_z$$

Supposing that the outer normal of the boundary is N and the cosine of its direction is n_x, n_y, n_z, the internal force of the elastomer on the boundary can be determined by the following formula:

$$
\begin{cases}
T_x = n_x \sigma_x + n_y \tau_{xy} + n_z \tau_{xz} \\
T_y = n_x \tau_{xy} + n_y \sigma_y + n_z \tau_{yz} \\
T_z = n_x \tau_{xz} + n_y \tau_{yz} + n_z \sigma_z
\end{cases}
$$

or

$$\{T\} = n\{\sigma\}$$

Among them:

$$
n = \begin{bmatrix}
n_x & 0 & 0 & n_y & 0 & n_z \\
0 & n_y & 0 & n_x & n_z & 0 \\
0 & 0 & n_z & 0 & n_y & n_x
\end{bmatrix}
$$

The displacement of the elastomer on Su is $\overline{u}, \overline{v}, \overline{w}$, hence:

$$u = \overline{u}, v = \overline{v}, w = \overline{w}$$

Where S_σ and S_u are the boundary conditions of the force and displacement.

Method References

38. K. Van den Eeckhout, A. J. J. Bos, D. Poelman & P. F. Smet, Revealing trap depth distributions in persistent phosphors. *Phys. Rev. B* **87**, 045126 (2013).
39. S. J. Clark *et al.*, First principles methods using CASTEP. *Z. Kristallogr.* **220**, 567-570 (2005).
40. L. Kleinman & D.M. Bylander, Efficacious Form for Model Pseudopotentials, *Phys. Rev. Lett.* **48**, 1425-1428 (1982).
41. S.G. Louie, S. Froyen & M.L. Cohen, Nonlinear ionic pseudopotentials in spin-density-functional calculations, *Phys. Rev. B* **26**, 1738-1742 (1982).
42. B. Huang, H. Dong, K.-L. Wong, L.-D. Sun & C.-H. Yan, Fundamental View of Electronic Structures of β-NaYF$_4$, β-NaGdF$_4$, and β-NaLuF$_4$, *J. Phys. Chem. C* **120**, 18858-18870 (2016).
43. B. Huang, Doping of RE ions in the 2D ZnO layered system to achieve low-dimensional upconverted persistent luminescence based on asymmetric doping in ZnO systems, *Phys. Chem. Chem. Phys.* **19**, 12683-12771 (2017).
44. M. Sun, H. Dong, A. W. Dougherty, Q. Lu, D. Peng, W. -T. Wong, B. Huang, L.-D. Sun, C.-H. Yan, Nanophotonic energy storage in upconversion nanoparticles, *Nano Energy* **56**, 473-481 (2019).
45. S. Hirata & M. Head-Gordon, Time-depenent density functional theory within the Tamm-Dancoff approximation, *Chem. Phys. Lett.* **314**, 291-299 (1999).